Journal of Thermal Analysis and Calorimetry (2018) 132:851–857
https://doi.org/10.1007/s10973-018-6969-5

Analysis of the sintering process in gadolinia-doped ceria by thermodilatometry and correlation with microstructure evolution

Rafael M. Batista[1] · E. N. S. Muccillo[1]

Received: 11 August 2017 / Accepted: 5 January 2018 / Published online: 22 January 2018

Abstract
The non-isothermal sintering process of cerium dioxide containing gadolinium sesquioxide powders within a wide range of specific surface area was investigated by dilatometry. Linear shrinkage data of powder compacts were recorded under several constant rates of heating. Dilatometry data were analyzed by two methodologies enabling to preview the relative density for any temperature/time profile, and determination of the apparent activation energy for sintering. Correlation of dilatometry results with microstructure evolution was also carried out. Remarkable differences in sintering powders with different specific surface areas were found. The apparent activation energy for sintering increases with decreasing specific surface area and, in most cases, it does not change significantly in the approximately 70–85% range of relative density.

Keywords Ceria · Sintering · Dilatometry · Modeling · Microstructure

Introduction

Solid solutions of cerium dioxide with rare earth oxides, especially gadolinium and samarium sesquioxides, are promising ceramic materials for application in electrochemical devices such as solid oxide fuel cells [1, 2]. It has been shown that 10 mol% gadolinium-doped cerium dioxide (hereafter GDC) displays the highest value of ionic conductivity among the rare earths [3].

The isothermal sintering of GDC in air [4, 5] as well as under inert and reducing atmospheres [6, 7] has been extensively investigated, due to its low sinterability, requiring temperatures of at least 1300 °C to attain high densification. Relatively few studies may be found on non-isothermal sintering based on thermodilatometry, or dilatometry, data [6, 8].

Dilatometry is a powerful technique that allows for obtaining reliable data on both physical and chemical properties of materials. This characterization technique finds wide application on phase transition studies [9], for determining the thermal expansion coefficient [10] in ceramics and themokinetics studies [11, 12].

In a previous work, the methodology for constructing the master sintering curve (MSC) was applied to dilatometry data obtained for nanostructured GDC to preview its density evolution [8]. In this work, the sintering process of GDC compacts prepared with powders within a wide range of specific surface area is investigated by dilatometry. The main purpose of this work was to evaluate the effects of the specific surface area on the sintering evolution of GDC. The linear shrinkage data were used to preview the sintering profile by construction of the MSC and to determine the apparent activation energy for sintering according to the constant rate of heating (CRH) method. The obtained results were correlated to the microstructure evolution.

Theoretical background

Two methodologies were exploited to investigate the sintering process using linear shrinkage data obtained from dilatometry: the construction of the MSC and the CRH method. A full account on these methodologies may be found elsewhere [13, 14]. In brief, these approaches are based on the combined-stage sintering model [13]. Assuming that a single densification mechanism

✉ Rafael M. Batista
morgadoph@gmail.com

[1] Center of Materials Science and Technology, Energy and Nuclear Research Institute - IPEN, PO Box 11049, São Paulo, SP 05422-970, Brazil

predominates and neglecting boundary diffusion, the densification rate of a powder compact may be written as:

$$\ln\left(\frac{T}{\rho}\frac{\mathrm{d}\rho}{\mathrm{d}t}\right) = \ln\left(\frac{3\gamma\Omega D_{0\mathrm{v}}\Gamma_{\mathrm{v}}}{kT \quad G^3}\right) - \frac{Q_{\mathrm{v}}}{kT} \tag{1}$$

where T is the absolute temperature, t the time, ρ the density, k the Boltzmann constant, γ the surface energy, Ω the atomic volume, G the mean grain size, $D_{0\mathrm{v}}$ the pre-exponential factor of the diffusion coefficient, Γ_{v} the lumped scaling parameter and Q_{v} the activation energy.

Presuming, in addition, that the mean grain size depends only on the density, the first term in the right-hand side of Eq. (1) becomes just a function of density. In this case, only volume diffusion was taken into account. Similar equation may be written for the boundary diffusion mechanism.

Construction of the MSC involves similar hypothesis than those for the CRH method. In this case, the rate of densification basic equation is rearranged and separated into two terms involving the microstructure and thermal history [14]. Then, the work of sintering is given by:

$$\Theta(t, T(t)) = \int_T^t \frac{1}{T}\exp\left(-\frac{Q}{RT}\right)\mathrm{d}t. \tag{2}$$

The work of sintering represents a measure of the energy supplied to the compact during sintering.

In this case, the analysis of the sintering process of GDC was carried out by applying Eqs. (1) and (2) to obtain the apparent activation energy for sintering and the MSC, respectively.

Experimental

Specimen preparation

$Ce_{0.9}Gd_{0.1}O_{2-\delta}$ (99.5%, Fuel Cell Materials, USA) powders with different specific surface areas, 7.4, 36.2 and 210 $m^2\ g^{-1}$, were used as received. Special care was taken during manipulation of these powders to avoid contamination. Cylindrical specimens with 5 mm diameter (ϕ) and 10–12 mm thickness (t) for dilatometry measurements were prepared without any additive by uniaxial (50 MPa) and cold isostatic (70 MPa) pressing. For conventional sintering, disk-shaped specimens (10 mm ϕ and 2–3 mm t) were prepared following the same procedure. Conventional sintering was carried out in air at 10 °C min^{-1} heating rate in a tube furnace (Lindberg BlueM). Dwell temperatures spanned from 600 to 1400 °C and holding times from 0 to 15 h. (Note: 0 stands for no holding time, i.e., the specimen was immediately cooled down to room temperature after reaching the dwell temperature.)

Dilatometry and data analysis

Linear shrinkage measurements were performed in a push-rod vertical dilatometer (Anter, Unitherm™ 1161) with nominal precision of 1 μm up to 1400 °C. These measurements were conducted in air with heating rates of 3, 6, 10 and 12 °C min^{-1} and cooling rate of 10 °C min^{-1}. The thermal expansion of the experimental set up was evaluated by measuring a translucent alumina (Crystalox®). The thermal expansion of GDC compacts was determined from the slope of the shrinkage-straight line recorded in the cooling process. Powders and sintered compacts are hereafter named according to the specific surface area of the starting powders as S1 (7.4 $m^2\ g^{-1}$), S2 (36.2 $m^2\ g^{-1}$) and S3 (210 $m^2\ g^{-1}$).

Dilatometry data were analyzed by software specially designed for construction of the MSC [15]. The software allows for application of several corrections to collected data such as the initial specimen length, initial temperature, mass loss and thermal expansions of the probe and specimen. Details on the procedures for these last corrections may be found elsewhere [8]. Evaluation of the apparent activation energy for sintering by the CRH method [16] was also implemented in the software. Density curves were obtained after application of the desired corrections to linear shrinkage and to the corresponding first-derivative curves.

Analysis of linear shrinkage by the CRH method consisted in obtaining the density curves from experimental data recorded with different constant rates of heating. Then, the term in the left-hand side of Eq. (1) was calculated for each curve for the same density value. The activation energy was determined from the slope of the linear fit of calculated values versus reciprocal absolute temperature plot.

For construction of the MSC, the density curves obtained with different constant heating rates were assumed to be represented by a sigmoid function and converted to density as a function of the work of sintering (Eq. 2). This procedure was performed for a preset value of Q. Afterward, the same procedure was repeated a number of times varying the value of Q and plotting the mean residual squares as a function of Q. The best value of Q corresponds to the one that minimizes the mean residual squares.

Specimen characterization

The microstructure of starting powders was observed by transmission electron microscopy, TEM (Jeol, JEM 2100) for determining the primary particle size using the ImageJ software. Structural analysis was carried out by X-ray

diffraction, XRD (Bruker-AXS, D8 Advance) with Cu Kα radiation and Ni filter in the 23–73° 2θ range with 0.04° step size and 5 s of counting time. Rietveld refinement with GSAS [17] was performed with experimental patterns to determine the crystallite size, the theoretical density and the microstrain. The mass loss was measured by thermogravimetry (Netzsch, STA 409E) under flowing synthetic air (5 mL min^{-1}) and alumina crucible, up to 1300 °C with 10 °C min^{-1} heating rate. The green and the apparent density of specimens sintered by the conventional method were calculated from measurements of specimen dimensions (micrometer Tesa, CH-1020) and mass (Mettler, H315).

Results and discussion

Powder characterization

Results obtained for powder and compacts S3 may be found elsewhere [8] and will not be stressed here, except for comparison purposes.

Figure 1 shows the XRD pattern of powder S1 along with results of Rietveld refinement. Small crosses in the bottom are the Bragg angular position of the cubic fluorite-type phase. The experimental pattern shows excellent agreement with the refined profile. Similar results were obtained for other powders. The lattice parameter and the theoretical density are 0.5420 nm and 7.21 g cm^{-3}, respectively. The microstrain (Table 1) is negligible for all powders, although there is a net tendency to increase with increasing specific surface area. Table 1 lists values of crystallite size determined from refinement of XRD patterns. The crystallite size increases with decreasing the specific surface area, as expected. Nevertheless, that

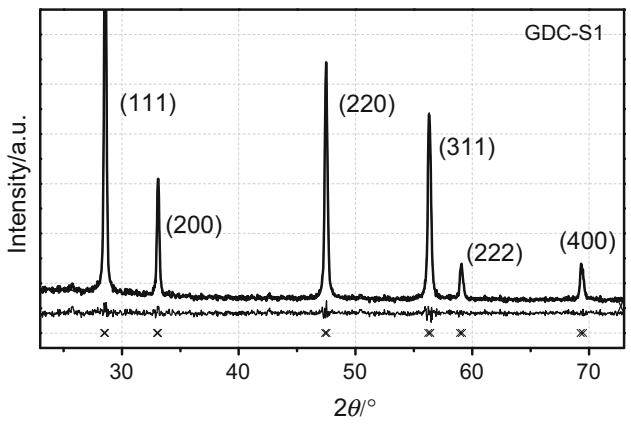

Fig. 1 XRD pattern of GDC powder S1 and Rietveld refinement. Residues (line below the XRD pattern) and angular position of the cubic fluorite-type reflections (crosses at the bottom)

increase in the crystallite size is non linear and is enhanced for decreasing the specific surface area.

Typical microstructure features of powder particles are shown by TEM micrographs in Fig. 2. The particles are polygonal in shape and exhibit some degree of agglomeration. Values of the mean primary particle size calculated by ImageJ software from several TEM micrographs are summarized in Table 1.

Good agreement was obtained between the primary particle and the crystallite sizes revealing that the powders are constituted by single crystals, although the initial size greatly differs.

The total mass loss up to 1300 °C is also listed in Table 1. It may be seen that mass loss increases with increasing the specific surface area of the starting powder. Most of mass loss takes place up to 200 °C for powders S1 and S2 and may be attributed to physisorbed water. The mass loss of powder S3 extends to ~ 700 °C and was found to be related to moisture and adsorbed CO_2 from the surrounding atmosphere [8].

Linear shrinkage

Figure 3a and b shows, respectively, the linear shrinkage and their first-derivative curves obtained for GDC compacts after corrections for thermal expansion of the probe and specimen. The onset temperature, T_{on}, for shrinkage (Fig. 3a) decreases with increasing the specific surface area of the starting powder. T_{on} for specimens S1 and S2 are approximately 940 and 680 °C, respectively. The temperature at which the shrinkage starts for S3 specimen could not be precisely determined because of the mass loss. The temperature of maximum shrinkage rate is 1250 °C for specimen S1 exhibiting a single maximum in the derivative curve (Fig. 3b). Specimen S2, in contrast, presented two overlapping maxima (920 and 1050 °C) in the first-derivative curve of the linear shrinkage. This powder shows no significant mass loss for temperatures above ~ 200 °C, and it is currently known that GDC did not exhibit any phase transition at such temperatures. Then, the two maxima in Fig. 3b might have been driven by concurrent mechanisms of sintering or by a bi-or multimodal distribution of particle sizes. For specimen S3, if we neglect data below 700 °C due to mass loss, then a single maximum at 850 °C is observed, as shown in Fig. 3b. The coefficient of thermal expansion (in 10^{-6} $°C^{-1}$) for these GDC specimens determined from linear shrinkage curves are 11.3 (S1), 13.9 (S2) and 19.4 (S3), in general agreement with previous reported data [16, 17].

Relative density curves for all compacts were plotted from corrected linear shrinkage data. Figure 4 shows, as example, the high temperature range of the density curve

Table 1 Characteristics of starting powders

Specimen	Microstrain/10^{-4}%	Crystallite size/nm	Primary particle size/nm	Mass loss/%
S1	–	72 (5)	82.1 (29)	<1.0
S2	0.3	14.9 (8)	12.4 (5)	2.5
S3	5.0	4.2 (3)	3.3 (2)	13

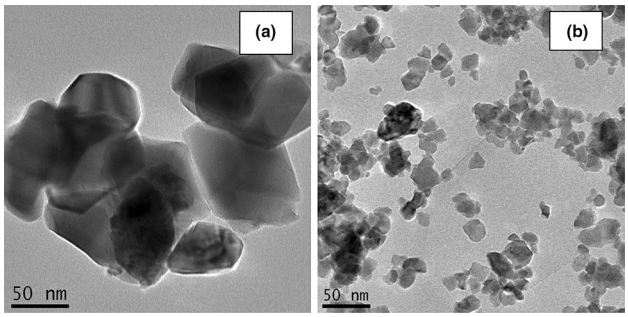

Fig. 2 Bright-field TEM micrographs of GDC powders **a** S1 and **b** S2

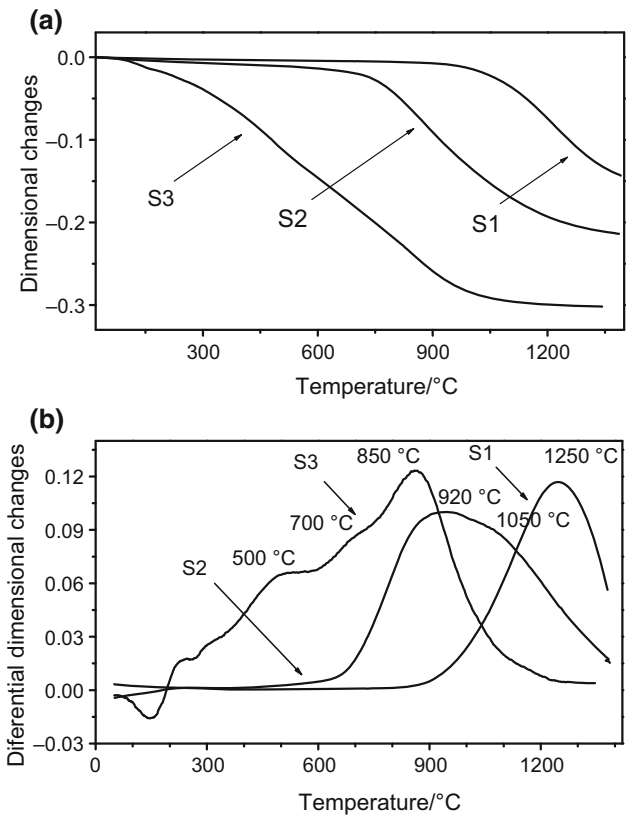

Fig. 3 **a** Linear shrinkage and **b** first-derivative curves of GDC compacts prepared with powders *S1*, *S2* and *S3* after corrections (heating rate = 10 °C min^{-1})

obtained for compacts prepared with powder S2 and recorded with several heating rates.

The relative density reached at any temperature was higher for the lower heating rate. Similar results were found for other ceramic materials and are explained taking

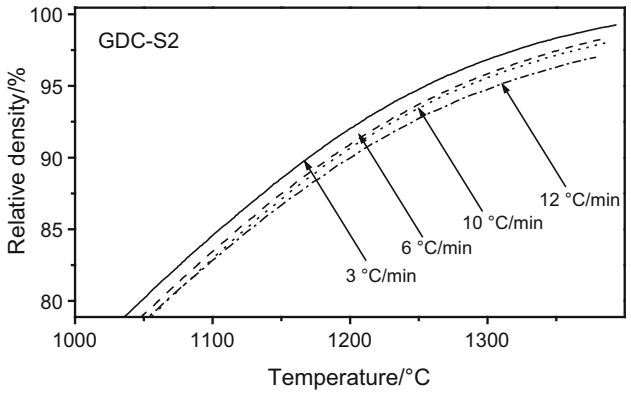

Fig. 4 High temperature range of relative density curves calculated from corrected shrinkage data of GDC compacts prepared with powder S2 at several heating rates

into account the large amount of thermal energy transferred to the compact when slow heating rates are used [14, 20]. Compacts prepared with powders S1 and S3 showed the same tendency.

Master sintering curve

Figures 5 and 6 show MSC of GDC compacts prepared with powders S1 (GDC-S1) and S2 (GDC-S2), respectively, with corrections of experimental data for thermal expansion of the probe and specimen, and mass loss. The whole density range was considered for these calculations. Linear shrinkage experiments were performed twice for GDC-S1 to ensure reproducibility, as shown in Fig. 5. The inset in Figs. 5a and 6a shows typical mean residual squares versus activation energy plots used to determine the best value of Q: 942 (GDC-S1), 834 (GDC-S2) and 576 kJ mol^{-1} (GDC-S3). The experimental data obtained with different heating rates exhibited excellent convergence in a wide range of log Θ. The MSC (solid line) fitted quite well the experimental data. Deviation of the MSC from the expected behavior at low and high log Θ may be a consequence of more than one mechanism of sintering acting simultaneously in these specific ranges, such as the grain growth at high log Θ values. Similar results were obtained for compacts prepared with powders S2 (Fig. 6) and S3 [8].

The validation of the MSC was performed with density values determined for GDC compacts isothermally and

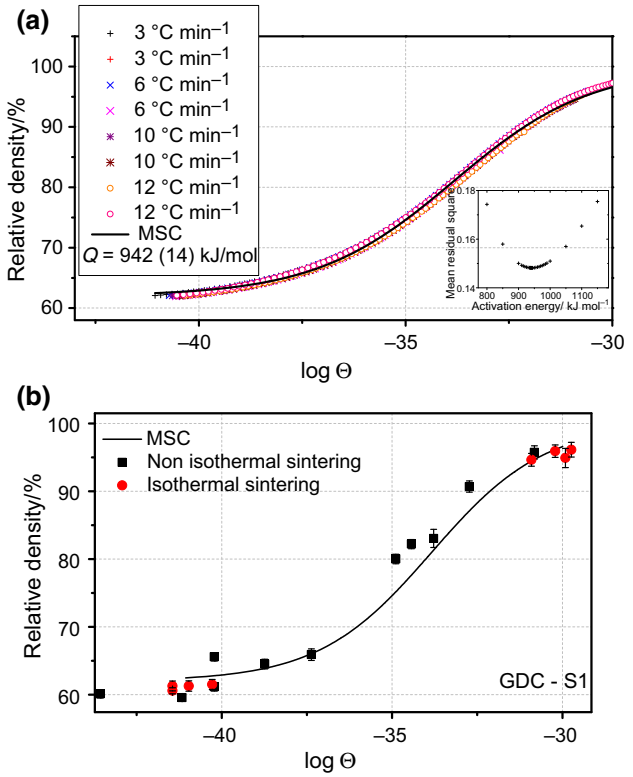

Fig. 5 MSC of GDC compacts prepared with powder S1. **a** Convergence of density data for several heating rates. Inset: mean residual squares versus activation energy. **b** validation of the MSC (continuous line) with density data obtained for conventionally sintered specimens (discrete points)

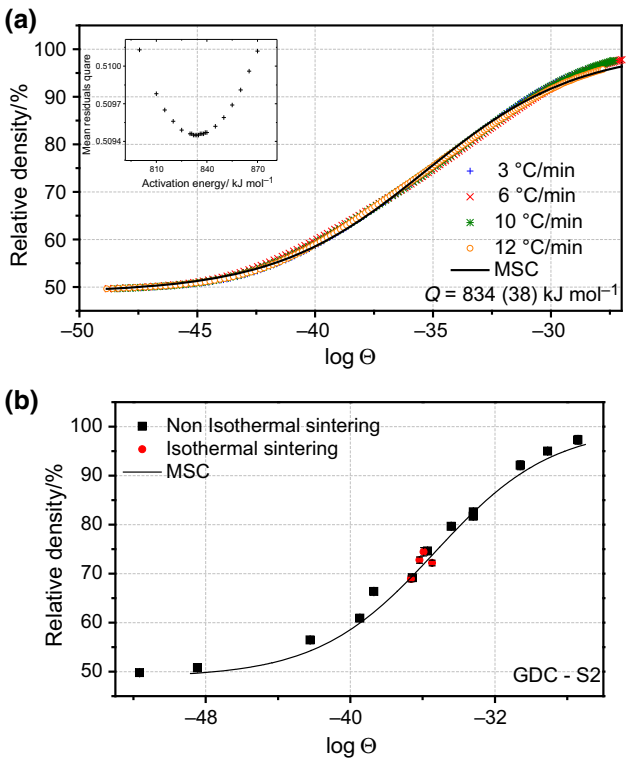

Fig. 6 MSC of GDC compacts prepared with powder S2. **a** Convergence of density data for several heating rates. Inset: mean residual squares versus activation energy. **b** validation of the MSC (continuous line) with density data obtained for conventionally sintered specimens (discrete points)

non-isothermally sintered by the conventional method (discrete points in Figs. 5b and 6b). The discrete point close to the origin in these plots is the green density. The good agreement between the MSC (solid line) and the discrete points exemplify the viability of using the MSC formalism for predicting density data.

Activation energy by the CRH method

The apparent activation energy for sintering of GDC compacts was determined from Arrhenius plots of the sintering data from ~ 60% to ~ 90% of relative density. In this method, as in the MSC formalism, it is assumed that the grain size is solely function of density. Figure 7 shows, as example, typical Arrhenius plots for GDC-S3.

The activation energy at a given density was determined from the slope of the linear fit of sintering data for that specific density. The good linear fit to the data for each relative density (Fig. 7) enables reasonable confidence on the calculated Q value. There is a single slope for the several straight lines in the ~ 64 to ~ 80% range of density. For higher relative densities, there is a change of slope with consequent changes in the value of Q. These changes of slope of the linear fit of sintering data are usually attributed to several factors, such as the distribution of particle size, or changes in the mass transport mechanism or in the relative weight of competing mechanisms [21]. In general, grain growth accounts for this effect at high relative densities. Similar Arrhenius plots were constructed for GDC-S1 and GDC-S2 compacts.

The evolution of activation energy values with density for GDC compacts is depicted in Fig. 8. GDC-S3 compacts (Fig. 8a) exhibit similar values of Q between ~ 65 and ~ 80% of relative density. GDC compacts prepared with powder S1 (Fig. 8c) also show a wide range of linearity of Q from about 70% to ~ 90% and decreases slightly for lower densities. In contrast, the behavior of Q for GDC-S2 compacts (Fig. 8b) reveals a different behavior with a maximum value at ~ 80% relative density. This effect is probably a consequence to that observed in the first-derivative curve of the linear shrinkage with overlapping maxima (Fig. 3b). In this case, the apparent activation energy for sintering determined from the mean residual squares plot for construction of the MSC (Fig. 6) may not be related to a specific sintering mechanism,

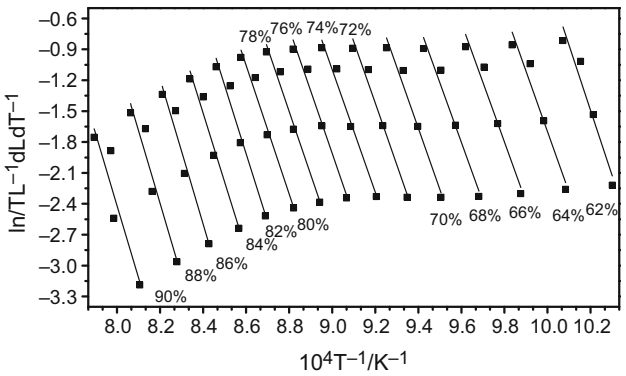

Fig. 7 Arrhenius plots of GDC-S3 for the estimate of activation energy for sintering via the CRH method

although represents an average value over the entire range of relative density.

The gradual increase in the apparent activation energy for sintering with decreasing the specific surface area of GDC compacts reflects the relative difficulty for densification of large-sized particles compared to nanostructured ones.

The activation energies for GDC determined by construction of the MSC are slightly higher than those calculated by the CRH method. The same effect has been previously reported [22, 23].

Microstructure evolution

Figure 9 shows the evolution of the crystallite size with (a) temperature and (b) density for sintered GDC. The compacts were thermally treated at several temperatures for null holding time. Points near the origin in Fig. 9a correspond to measurements carried out in as-received powders. The crystallite growth is sluggish up to approximately 1200 °C for all GDC specimens, and for higher temperatures it grows exponentially. It may be seen that the initial crystallite size is higher for GDC-S1, although it grows slowly in the 1000–1200 °C range, as shown in Fig. 9a.

The evolution of the crystallite size with density is similar for GDC-S2 and GDC-S3, as shown in Fig. 9b. At low relative densities, the crystallite size growth was slow, and it was increasingly accelerated with increasing density, in general agreement with the temperature dependence shown in Fig. 9a. It is worth noting that in the beginning of the sintering process, the crystallite size of GDC-S1 increased, but the relative density remained constant. This behavior is typical of non-densifying sintering mechanisms like surface diffusion and vapor transport [24]. The former has low activation energy and is expected to contribute to mass transport at temperatures below that of the initial shrinkage [21]. The existence of a non-densifying mechanism of sintering for GDC-S1 with low activation energy explains the decrease in the value of Q for relative densities lower than 70% (Fig. 8b).

Summary

The sintering process of GDC compacts prepared from powders with a wide range of specific surface area was investigated by dilatometry. Powder characterization reveals that GDC powders are constituted by single crystalline particles of different sizes. The coefficient of

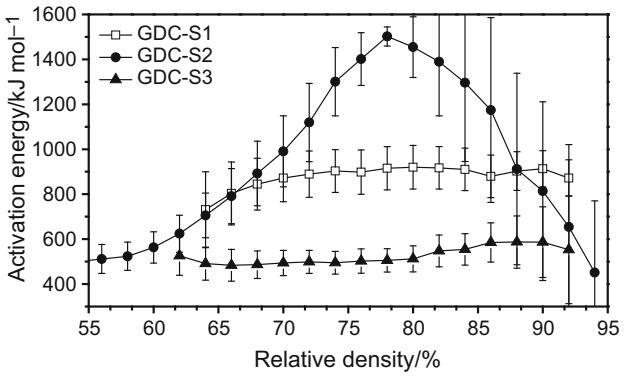

Fig. 8 Evolution of Q with the relative density for GDC compacts prepared with powders *S1*, *S2* and *S3*

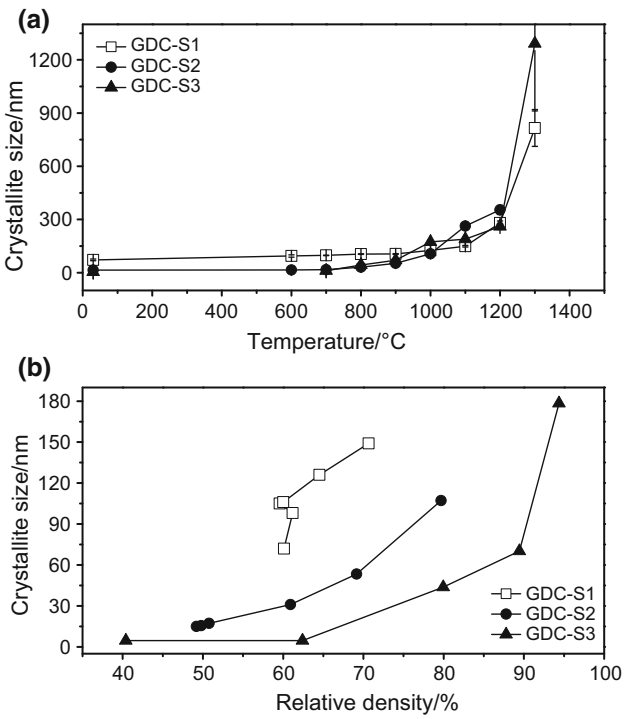

Fig. 9 Evolution of the crystallite size of GDC compacts with the **a** temperature and **b** relative density

thermal expansion determined from linear shrinkage curves agrees with previous reported values ($\sim$ 11–19 10^{-6} °C^{-1}). The mass loss decreases with decreasing the specific surface area of GDC powder. The T_{onset} in dilatometry experiments reduces drastically with increasing the specific surface area, whereas the final density achieved by GDC compacts does not depend on that parameter. The MSC of GDC compacts was constructed and validated by density values determined for conventionally sintered specimens. The activation energy for sintering was determined for GDC compacts by the CRH method in the whole extension of relative densities, allowing for determining the range of density where that value is constant. Both methodologies give reliable information on the sintering process of GDC compacts. The higher the specific surface area, the higher the apparent activation energy for sintering. Evaluation of the growth of crystallite size with temperature and density enables explaining sintering features, such as the existence of a non-densifying mechanism in GDC compacts prepared with the powder of low specific surface area. The overall results indicate that reasonable understand of the sintering process of ceramic powders may be achieved by combination of sintering models and microstructure evolution.

Acknowledgements The authors acknowledge FAPESP (2013/07296-2), CNPq (Proc. no. 304073/2014-8) and CNEN for financial supports, and the Laboratory of Electron Microscopy at IPEN for TEM observation. One of the authors (R.M.B.) acknowledges Capes for the scholarship.

References

1. Yahiro H, Eguchi Y, Eguchi K, Arai H. Oxygen-ion conductivity of the ceria-samarium oxide system with fluorite structure. J Appl Electrochem. 1988;18:527–31.
2. Yahiro H, Eguchi K, Arai H. Electrical properties and reducibilities of ceria-rare earth oxide systems and their application to solid oxide fuel cell. Solid State Ion. 1989;36:71–5.
3. Steele BCH, Heinzel A. Materials for fuel-cell technologies. Nature. 2001;414:345–52.
4. Inaba H, Nakajima T, Tagawa H. Sintering behaviors of ceria and gadolinia-doped ceria. Solid State Ion. 1998;106:263–8.
5. Jurado JR. Present several items on ceria-based ceramic electrolytes: synthesis, additive effects, reactivity and electrochemical behavior. J Mater Sci. 2001;36:1133–9.
6. He Z, Yuan H, Glasscock JA, Chatzichristodoulou C, Phair JW, Kaiser A, Ramousse S. Densification and grain growth during early-stage sintering of $Ce_{0.9}Gd_{0.1}O_{1.95-\delta}$ in a reducing atmosphere. Acta Mater. 2010;58:3860–6.
7. Batista RM, Ferreira AMDC, Muccillo ENS. Sintering and electrical conductivity of gadolinia-doped ceria. Ionics. 2016; 22:1159–66.
8. Batista RM, Muccillo ENS. Dilatometry analysis of the sintering process of nanostructured gadolinia-doped ceria. J Therm Anal Calorim. 2016;126:1007–13.
9. Malghe YS, Dharwadkar SR, Krishnan K, Mudher KDS. Dilatometry and high temperature X-ray diffractometry study of $LaCrO_3$ prepared using microwave heating. J Therm Anal Calorim. 2009;95:49–52.
10. Durrani SK, Naz S, Nadeem M, Khan AA. Thermal, structural and impedance analysis of nanocrystalline magnesium chromite spinel synthesized via hydrothermal process. J Therm Anal Calorim. 2014;116:309–20.
11. Surzhikov AP, Ghyngazov SA, Frangulyan TS, Vasil'ev IP, Chernyavskii AV. Investigation of sintering behaviour of ZrO_2 (Y) ceramic green body by means of non-isothermal dilatometry and thermokinetic analysis. J Therm Anal Calorim. 2017;128: 787–94.
12. Erceg M, Krešić I, Jakić M, Andričić B. Kinetic analysis of poly(ethylene oxide)/lithium montmorillonite nanocomposites. J Therm Anal Calorim. 2017;127:789–97.
13. Hansen J, Rusin RP, Teng M, Johnson DL. Combined-stage sintering model. J Am Ceram Soc. 1992;75:1129–35.
14. Su H, Johnson DL. Master sintering curve: a practical approach to sintering. J Am Ceram Soc. 1996;79:3211–7.
15. Batista RM, Naranjo JFR, Muccillo ENS. A versatile software for construction of the máster sintering curve. Mater Sci Forum. 2018;912:240–4.
16. Wang J, Raj R. Estimate of activation energies for boundary diffusion from rate-controlled sintering of pure alumina, and alumina doped with zirconia or titania. J Am Ceram Soc. 1990;73:1172–5.
17. Larson AC, Deele RB von. General structure analysis system (GSAS), Los Alamos National Laboratory Report LAUR 86-748, 1994.
18. Kudo T, Obayashi H. Oxygen ion conduction of the fluorite-type $Ce_{1-x}Ln_xO_{2-x/2}$ (Ln = Lanthanoid element). J Electrochem Soc. 1975;122:142–7.
19. Kharton VV, Figueiredo FM, Navarro L, Naumovich EN, Kovalevsky AV, Yaremchenko AA, Viskup AP, Carneiro A, Marques FMB, Frade JR. Ceria-based materials for solid oxide fuel cells. J Mater Sci. 2001;36:1105–17.
20. Ewsuk KG, Ellerby DT, DiAntonio CB. Analysis of nanocrystalline and microcrystalline ZnO sintering using master sintering curves. J Am Ceram Soc. 2006;89:2003–9.
21. Young WS, Cutler IB. Initial sintering with constant rates of heating. J Am Ceram Soc. 1970;53:659–63.
22. Aminzare M, Mazaheri M, Golestani-fard F, Rezaie HR, Ajeian R. Sintering behavior of nano alumina powder shaped by pressure filtration. Ceram Int. 2011;37:9–14.
23. Rajeswari K, Padhi S, Reddy ARS, Johnson R, Das D. Studies on sintering kinetics and correlation with the sinterability of 8Y zirconia ceramics based on the dilatometric shrinkage. Ceram Int. 2013;39:4985–90.
24. Rahaman MN. Sintering of ceramics. Boca Raton: CRC Press; 2008.